Journal of Physics D: Applied Physics

PAPER

Enhanced performance of GaAs-based betavoltaic batteries by using AlGaAs hole/electron transport layers

To cite this article: Renzhou Zheng *et al* 2022 *J. Phys. D: Appl. Phys.* **55** 304002

View the article online for updates and enhancements.

You may also like

- Investigation of a temperature tolerant InGaP (GaInP) converter layer for a ^{63}Ni betavoltaic cell
S Butera, M D C Whitaker, A B Krysa et al.
- Analytical Study of ^{90}Sr Betavoltaic Nuclear Battery Performance Based on p-n Junction Silicon
Swastya Rahastama and Abdul Waris
- A high open-circuit voltage gallium nitride betavoltaic microbattery
Zaijun Cheng, Xuyuan Chen, Haisheng San et al.

This content was downloaded from IP address 159.226.165.22 on 07/02/2023 at 01:02

IOP Publishing Journal of Physics D: Applied Physics
J. Phys. D: Appl. Phys. **55** (2022) 304002 (9pp) https://doi.org/10.1088/1361-6463/ac6c5c

Enhanced performance of GaAs-based betavoltaic batteries by using AlGaAs hole/electron transport layers

Renzhou Zheng[1], Jingbin Lu[1,*], Yu Wang[1], Lei Liang[2,3,4,*], Yugang Zeng[2], Li Qin[2], Yongyi Chen[2], Xue Zhang[1], Ziyi Chen[1], Xiaoyi Li[1], Xinxu Yuan[1] and Yumin Liu[5]

[1] College of Physics, Jilin University, Changchun 130012, People's Republic of China
[2] State Key Laboratory of Luminescence and Applications, Changchun Institute of Optics, Fine Mechanics and Physics, Chinese Academy of Sciences, Changchun 130033, People's Republic of China
[3] Center of Materials Science and Optoelectronics Engineering, University of Chinese Academy of Sciences, Beijing 100049, People's Republic of China
[4] Peng Cheng Laboratory, No. 2, Xingke 1st Street, Shenzhen 518000, People's Republic of China
[5] College of Nuclear Science and Engineering, East China University of Technology, Nanchang 330013, People's Republic of China

E-mail: ljb@jlu.edu.cn and liangl@ciomp.ac.cn

Received 25 January 2022, revised 13 April 2022
Accepted for publication 3 May 2022
Published 13 May 2022

Abstract

The GaAs-based betavoltaic batteries with ^{63}Ni source were demonstrated, in which the AlGaAs hole/electron transport layers were introduced to enhance the transport and collection of radiation-induced carriers. The Monte Carlo codes and COMSOL Multiphysics were combined to predict the output performance of batteries and optimize the structure parameters of energy converter. And the optimized GaAs-based battery with a 6 mCi cm^{-2} ^{63}Ni source was expected to achieve a short-circuit current density (J_{sc}) of 85.6 nA cm^{-2}, an open-circuit voltage (V_{oc}) of 0.67 V and a maximum output power density (P_m) of 43.3 nW cm^{-2}. Then the GaAs/AlGaAs films were grown by metal organic chemical vapor deposition, and the comb-like electrodes were designed to reduce the absorption loss of beta particles in the p-plane electrode. The photoluminescence and x-ray diffraction were carried out to characterize the growth quality of epitaxial materials. The experimental results showed that the largest J_{sc} of 9.3 nA cm^{-2}, V_{oc} of 55 mV and P_m of 143.9 pW cm^{-2} can be achieved on the 2-busbar electrode battery. And the temperature dependence tests showed that when the temperature decreased to 233.15 K, the V_{oc} and P_m increased to 208 mV and 570.5 pW cm^{-2}, respectively. Further improvements in fabrication process are needed to reduce the gap between experiment and prediction. In addition, the optimized structure of energy converter suggests the directions for enhancing the performance of betavoltaic batteries.

Keywords: betavoltaic battery, GaAs, Monte Carlo, COMSOL simulation, MOCVD

(Some figures may appear in colour only in the online journal)

* Authors to whom any correspondence should be addressed.

 © 2022 IOP Publishing Ltd

1. Introduction

As a type of nuclear batteries, the betavoltaic batteries can convert the decay energy of beta radioisotopes into electrical energy with long service life, high power density, small scale and strong environmental adaptability [1, 2]. These make the betavoltaic batteries an appropriate option for powering the micro-electro-mechanical-systems. When the beta particles interact with the semiconductor energy converter, a p–n junction or a Schottky barrier diode, thousands of electron–hole pairs are generated. And they can be collected to form the radiation-induced current, the process of which is similar to a photovoltaic battery. Recent studies have shown that the betavoltaic batteries have been successfully used in deep-space exploration, remote site, execrable ambient and medical applications [3, 4].

The performance of a betavoltaic battery depends on many factors, such as radioisotope characteristics, energy converter structure and semiconductor material properties [5, 6]. The maximum beta energy of ^{3}H and ^{63}Ni source are 18.6 and 66.9 keV, respectively, and their average beta energy are 5.7 and 17.4 keV, respectively [7]. They can meet the requirement of almost no radiation damage to the semiconductors. And the longer half-life of 100.2 years makes the ^{63}Ni source the most appropriate choice for the betavoltaic devices. Theoretical studies have shown that the energy conversion efficiency of a betavoltaic battery increase with the increase of semiconductor band gap [8]. Compared with the tradition Si semiconductor, GaAs has the wider band gap (1.424 eV), higher electron mobility ($\sim$8000 cm^2 (V·s)$^{-1}$), lower intrinsic carrier concentration (1.8×10^6 cm^{-3}) and higher threshold energy for radiation damage (270 keV) [9]. The GaAs-based betavoltaic batteries are expected to have satisfactory performance, and have also been reported [10–18]. In 2012, a GaAs betavoltaic battery based on P$^+$PINN$^+$ structure was proposed [14]. The added interlayer in typical PIN structure enlarged the width of depletion region and enhanced the collection of minority carriers. As a result, compared to the typical PIN structure, the conversion efficiency of battery improved by 45% and a short-circuit current density of 0.36 nA cm^{-2} was obtained. In 2015, the temperature effects on the output performance of ^{63}Ni-GaAs and ^{147}Pm-GaAs betavoltaic batteries were investigated [15]. Both the theoretical and experimental results showed that the open-circuit voltage of battery decreased with the increase of temperature. And at 213.15 K, the largest experimental values of open-circuit voltage of the ^{63}Ni-GaAs and ^{147}Pm-GaAs batteries were 0.47 and 0.41 V, respectively. In 2017, the temperature effects were studied by another group, and a maximum output power density of 1.4 nW cm^{-2} of the ^{63}Ni-GaAs battery were observed at -20 °C [16]. In 2019, an energy converter based on the AlGaAs/GaAs heterostructure was presented. Under the irradiation of a tritium gas source, the battery achieved an efficiency of 5.9% [17]. In 2022, a GaAs-based battery with Schottky structure modified by deposition of a carbon layer was investigated. Their experiments and simulations showed that the carbon deposition at the top of n-GaAs layer can passivate the surface state of GaAs, and further improve the battery performance [18].

Nevertheless, from these experimental reports, the output performances of the GaAs-based betavoltaic batteries are not excellent as expected. The short-circuit current density is only a few nanoamperes per square centimeter, and the maximum output power density is only a few nanowatts per square centimeter. The most important reason is that the band structure of device is not the most favorable for the transport and collection of radiation-induced carriers, and it lacks a certain auxiliary material unit. Thus the concepts of hole transport-electron blocking layers and electron transport-hole blocking layers are proposed, which significantly enhance the symmetry-breaking regions [19]. They can block one kind of carrier in favor of the other, and facilitate the movement of one kind of carrier in the opposite direction of the other. As a result, the recombination probability of carriers is reduced and they can be collected more efficiently. On the other hand, in recent studies, the structure designs of energy converter are based on the theoretical calculations with analytical expressions, and these expressions are obtained by solving the minority carrier diffusion equation and making a lot of hypotheses [13, 20, 21]. The prediction of battery performance and optimization of device structure are not as satisfactory as in the solar cell designs, where the device simulators, such as technology computer-aided design and COMSOL Multiphysics are used [22, 23].

Our previous work developed a simulation model to predict the output performance of the betavoltaic batteries, in which the Monte Carlo codes and COMSOL Multiphysics are combined [24]. In this study, we proposed the GaAs-based betavoltaic batteries with AlGaAs hole/electron transport layers, which have more favorable band structure for the transport and collection of radiation-induced carriers. After optimizing the structure parameters of energy converter theoretically, including the thickness, doping concentration and Al mole fraction of each layer, the batteries were demonstrated in our laboratory. The GaAs/AlGaAs films were grown by metal organic chemical vapor deposition (MOCVD), and a ^{63}Ni source was loaded to fabricate the betavoltaic batteries. Four kinds of comb-like electrodes were designed for the batteries, which can reduce the absorption loss of beta particles in the p-plane electrode. To characterize the battery performance, the effects of bus-bar number and temperature on the current–voltage (I–V) characteristics, short-circuit current density (J_{sc}), open-circuit voltage (V_{oc}) and maximum output power density (P_m) were investigated. These results suggest the directions for improving the performance of GaAs-based betavoltaic batteries and can be extended to other combinations of semiconductor and radioisotope.

2. Device structure and optimization design

As shown in figure 1, the proposed GaAs-based battery has six layers: a p$^+$-GaAs cap layer, a p-Al$_x$Ga$_{1-x}$As window layer, a p-GaAs emitter layer, an n-GaAs base layer, an n-Al$_x$Ga$_{1-x}$As back surface layer and an n-GaAs buffer layer. The p$^+$-GaAs cap layer is heavily doped for better metal

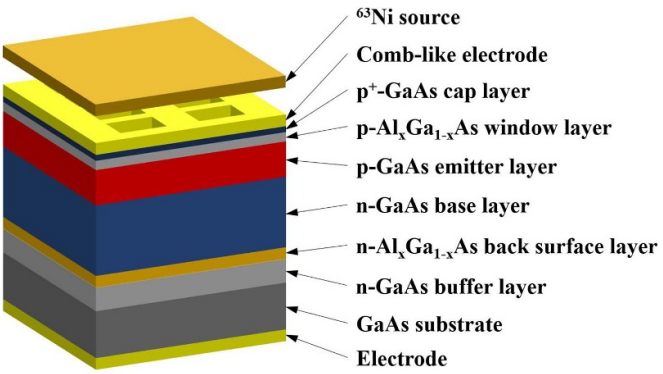

Figure 1. Structure of the GaAs-based betavoltaic battery.

contact. The p-Al$_x$Ga$_{1-x}$As window layer, as a hole transport layer, can reflect back the radiation-induced minority electrons diffused into the interface, thus reducing the battery surface recombination [25, 26]. The p-GaAs emitter layer and n-GaAs base layer are the core regions for a betavoltaic battery, where the radiation-induced electron–hole pairs are separated by the internal electric field. The n-Al$_x$Ga$_{1-x}$As back surface layer, as an electron transport layer, can reduce the recombination probability of the back surface by reflecting the radiation-induced minority holes back to the base layer and emitter layer. To optimize the structure parameters of the energy converter, including the thickness, doping concentration and Al mole fraction of each layer, the Monte Carlo codes and COMSOL Multiphysics are combined to predict the output performance of batteries.

The Monte Carlo codes are used to simulate the energy deposition distribution of ^{63}Ni source beta particles in GaAs and Al$_x$Ga$_{1-x}$As materials. Further, the electron–hole pairs generation rate can be calculated by using the Klein Formula, the average energy dissipated per electron–hole pair generated is $E_{ehp} = 2.8\ E_g$+0.5 eV, where E_g is the band gap of the semiconductor [27]. In our simulation model, a rectangular ^{63}Ni source (apparent activity density of 6 mCi cm^{-2}) with full energy spectrum is used to simulate the energy deposition along the radiation transport depth in GaAs and Al$_x$Ga$_{1-x}$As bulks. And the electron–hole pairs generation rate $G_1(Y)$ ($G_2(Y)$) in GaAs (Al$_x$Ga$_{1-x}$As), as a function of radiation transport depth Y, can be expressed as:

$$G_1(Y) = \frac{E_1(Y)}{E_{ehp(\mathrm{GaAs})}} = \frac{G_{01}\exp(-\alpha_1 Y)}{2.8E_{g1} + 0.5\ \mathrm{eV}}, \tag{1}$$

$$G_2(Y) = \frac{E_2(Y)}{E_{ehp(\mathrm{AlGaAs})}} = \frac{G_{02}\exp(-\alpha_2 Y)}{2.8E_{g2} + 0.5\ \mathrm{eV}}, \tag{2}$$

where $E_1(Y)$ ($E_2(Y)$) is the energy deposition rate in GaAs (Al$_x$Ga$_{1-x}$As) material, G_{01}, G_{02}, α_1 and α_2 are the exponential fitting parameters, E_{g1} is the band gap of GaAs (1.424 eV), E_{g2} is the band gap of Al$_x$Ga$_{1-x}$As, which is a function of Al mole fraction x [28]:

$$E_{g2} = \begin{cases} 1.424 + 1.247x\,(\mathrm{eV}), & x \leqslant 0.45 \\ 1.9 + 0.125x + 0.143x^2\,(\mathrm{eV}), & x > 0.45. \end{cases} \tag{3}$$

To be specific, $E_1(Y)$ can be expressed as:

$$E_1(Y) = 0.47275\exp(-0.10229\,Y)\ \mu\mathrm{W}{\cdot}\mu\mathrm{m}^{-1}{\cdot}\mathrm{cm}^{-2}, \tag{4}$$

where Y is in the units of μm. And then, $G_1(Y)$ is expressed as:

$$G_1(Y) = 6.5929\exp(-0.10229\,Y) \times 10^{21}\,\mathrm{m}^{-3}{\cdot}\mathrm{s}^{-1}. \tag{5}$$

Similarly, $G_2(Y)$ can be expressed as:

$$G_2(Y) = \begin{cases} \dfrac{2.9510\exp(-0.10229\,Y)}{2.8 \times (1.424 + 1.247x) + 0.5} \\ \quad \times 10^{22}\,(\mathrm{m}^{-3}{\cdot}\mathrm{s}^{-1}), x \leqslant 0.45 \\ \dfrac{2.9510\exp(-0.10229\,Y)}{2.8 \times (1.9 + 0.125x + 0.143x^2) + 0.5} \\ \quad \times 10^{22}\,(\mathrm{m}^{-3}{\cdot}\mathrm{s}^{-1}), x > 0.45. \end{cases} \tag{6}$$

As a result, the electron–hole pairs generation rate in GaAs and Al$_x$Ga$_{1-x}$As materials is a function of radiation transport depth Y and Al mole fraction x. It should be mentioned that the effect of Al mole fraction x on energy deposition distribution is ignored, and only the effects to band gap and average energy dissipated per electron–hole pair generated are considered. Then, in COMSOL calculations, the electron–hole pairs generation rate $G_1(Y)$ and $G_2(Y)$ can be defined in GaAs and Al$_x$Ga$_{1-x}$As materials, respectively.

The proposed GaAs-based batteries are modeled by the COMSOL Multiphysics, where the coupled Poisson and carrier continuity equations are solved to simulate the carrier transport and collection [29, 30]:

$$\nabla^2 V = -\frac{\rho}{\epsilon_0 \epsilon_r}, \tag{7}$$

$$-\frac{1}{q}\nabla j_n = G - R_n, \tag{8}$$

$$\frac{1}{q}\nabla j_p = G - R_p, \tag{9}$$

where V is the electrostatic potential, ρ is the charge density, ϵ_0 is the vacuum permittivity, ϵ_r is the relative permittivity of the material, q is the electron charge, G is the electron–hole pairs generation rate, R_n (R_p) is the electron (hole) recombination rate. And j_n (j_p) is the electron (hole) current density, which can be expressed as:

$$j_n = -\frac{\mu_n kT}{q}\nabla n + \mu_n n \nabla V, \tag{10}$$

$$j_p = -\frac{\mu_p kT}{q}\nabla p - \mu_p p \nabla V, \tag{11}$$

where μ_n (μ_p) is the electron (hole) mobility, k is the Boltzmann's constant, T is the absolute temperature, and n (p) is the electron (hole) concentration.

As reported in our previous work, various physical models are introduced in the simulations, including the analytic doping model, the low-field mobility model and the Shockley–Read–Hall (SRH) recombination model [24, 31, 32]. The current density–voltage (J–V) characteristics of the batteries can be obtained by sweeping the forward voltage across the device and recording the terminal current. In order to maximize the output power density and optimize the structure parameters of energy converter, the parametric sweep is used to tune the variables, including the thicknesses and doping concentrations of the p^+-GaAs cap layer ($H_{\text{cap layer}}$ and $N_{\text{cap layer}}$), p-$Al_xGa_{1-x}As$ window layer ($H_{\text{window layer}}$ and $N_{\text{window layer}}$), p-GaAs emitter layer ($H_{\text{emitter layer}}$ and $N_{\text{emitter layer}}$), n-GaAs base layer ($H_{\text{base layer}}$ and $N_{\text{base layer}}$), n-$Al_xGa_{1-x}As$ back surface layer ($H_{\text{back surface layer}}$ and $N_{\text{back surface layer}}$) and n-GaAs buffer layer ($H_{\text{buffer layer}}$ and $N_{\text{buffer layer}}$). And also the Al mole fraction x_1 of the p-$Al_xGa_{1-x}As$ window layer, the Al mole fraction x_2 of the n-$Al_xGa_{1-x}As$ back surface layer. The optimization processes are: first, setting a group of appropriate initial values for each structure parameter; second, calculating the maximum output power density (P_m) of batteries with a variation of structure parameters, and when one of the structure parameters changes, the other parameters are fixed as the initial values; then, determining the optimal value for each structure parameter; next, taking the optimization results of the first round as the initial values for the second round; after several rounds of calculation, the final optimization values of structure parameter can be determined.

Figure 2(a) shows the effects of $H_{\text{emitter layer}}$ and $H_{\text{base layer}}$ on P_m, and the $H_{\text{cap layer}}$, $H_{\text{window layer}}$, $H_{\text{back surface layer}}$ and $H_{\text{buffer layer}}$ values (optimized values) are 0.05 μm, 0.08 μm, 0.3 μm and 1 μm, respectively. As the core regions of the energy converter, the thicknesses of the emitter layer and base layer have a great effect on the battery performance. When the $H_{\text{emitter layer}}$ is larger than 1.5 μm, the P_m begins to decrease because the depletion region is away from the region of high electron–hole pairs generation rate. While as the $H_{\text{base layer}}$ increases, the P_m is almost constant. Figure 2(b) shows the effects of $N_{\text{cap layer}}$, $N_{\text{window layer}}$, $N_{\text{emitter layer}}$, $N_{\text{base layer}}$ and $N_{\text{back surface layer}}$ on P_m, and the $N_{\text{buffer layer}}$ value is set to $1 \times 10^{16}\,\text{cm}^{-3}$. Increasing the $N_{\text{cap layer}}$ is beneficial to the ohmic contact, while too high doping concentration results in the reduction of effective carrier concentration, which will lead to the degradation of battery performance. When the $N_{\text{window layer}}$ increases, the valance band in the p-$Al_xGa_{1-x}As$ window layer goes up, and the enhanced hole transport can improve the P_m. Obviously, the doping concentrations of the emitter layer and base layer have the greatest effect on P_m. The larger $N_{\text{emitter layer}}$ and $N_{\text{base layer}}$ are beneficial to form the higher built-in potential barrier, which can enhance the open-circuit voltage of battery. While the increase of doping concentrations decreases the depletion region width. Thus, the P_m first increases and then decreases. When the n-$Al_xGa_{1-x}As$ back surface layer is heavily doped, the conductor band and valance band go down, this is beneficial to the transport of electrons to the back surface and to reduce the recombination of holes on the back surface. After several rounds of calculation,

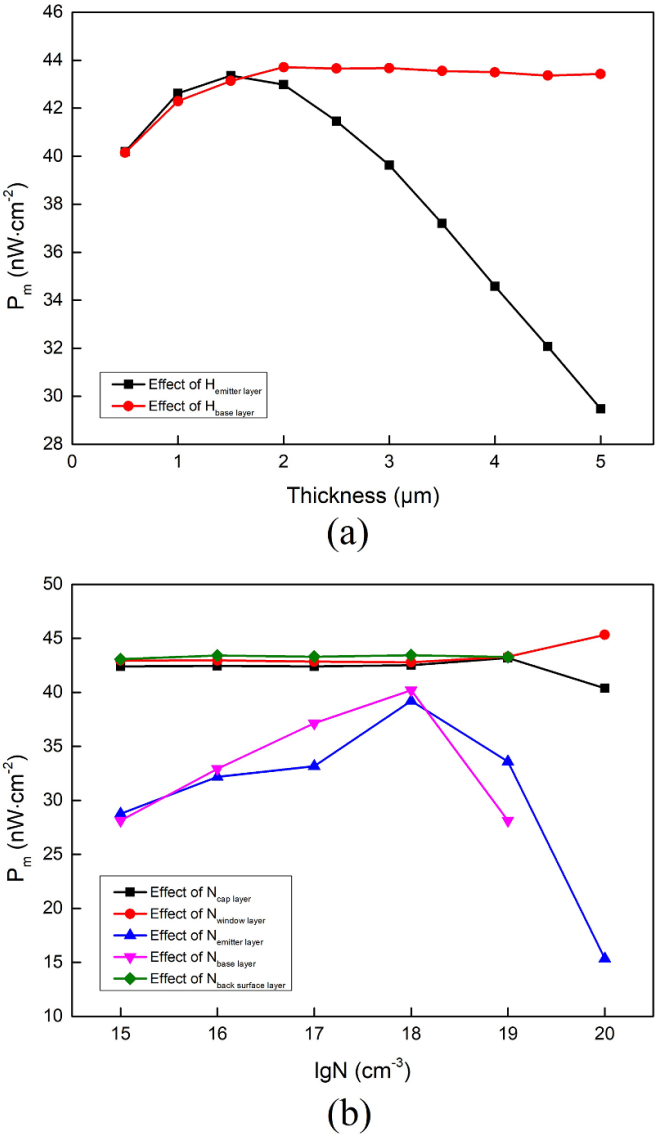

Figure 2. (a) Effects of $H_{\text{emitter layer}}$ and $H_{\text{base layer}}$ on P_m. (b) Effects of $N_{\text{cap layer}}$, $N_{\text{window layer}}$, $N_{\text{emitter layer}}$, $N_{\text{base layer}}$ and $N_{\text{back surface layer}}$ on P_m. The $H_{\text{cap layer}}$, $H_{\text{window layer}}$, $H_{\text{back surface layer}}$ and $H_{\text{buffer layer}}$ values are 0.05 μm, 0.08 μm, 0.3 μm and 1 μm, respectively. The $N_{\text{buffer layer}}$ value is $1 \times 10^{16}\,\text{cm}^{-3}$.

considering the energy band structure of device and the relationships between the output parameters and structure parameters, the optimized structure parameters of the GaAs-based batteries are finally determined, as listed in table 1. It should be mentioned that in our optimization processes, a smaller parametric sweep step is used to improve the accuracy of results.

Figure 3 shows the simulated current density–voltage (J–V) and power density–voltage (P–V) characteristics of the batteries with and without AlGaAs hole/electron transport layers. The short-circuit current density (J_{sc}) and open-circuit voltage (V_{oc}) of the battery with AlGaAs hole/electron transport layers are 85.6 nA cm^{-2} and 0.67 V, respectively. And the maximum output power density (P_m) can reach to 43.3 nW cm^{-2},

Table 1. The optimized structure parameters of the GaAs-based betavoltaic batteries.

Layer	Material	Thickness (μm)	Doping concentration (cm^{-3})
Cap layer	p^+-GaAs	0.05	2.00×10^{19}
Window layer	p-$Al_{0.85}Ga_{0.15}As$	0.08	1.00×10^{19}
Emitter layer	p-GaAs	1.5	2.51×10^{18}
Base layer	n-GaAs	4.5	7.94×10^{17}
Back surface layer	n-$Al_{0.25}Ga_{0.75}As$	0.3	1.00×10^{19}
Buffer layer	n-GaAs	1	1.00×10^{16}

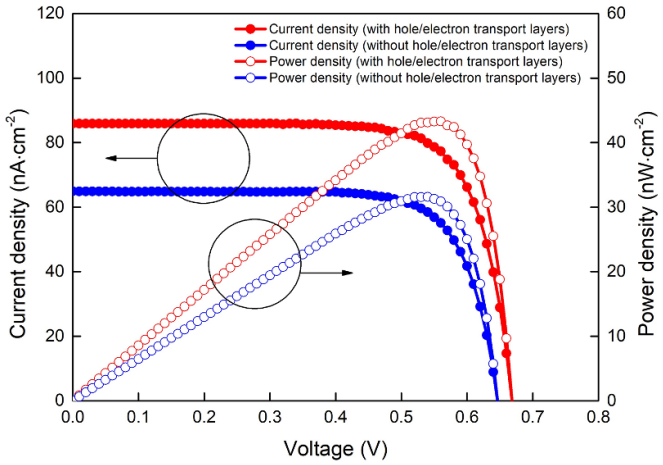

Figure 3. Simulated *J–V* and *P–V* characteristics of the batteries with and without AlGaAs hole/electron transport layers.

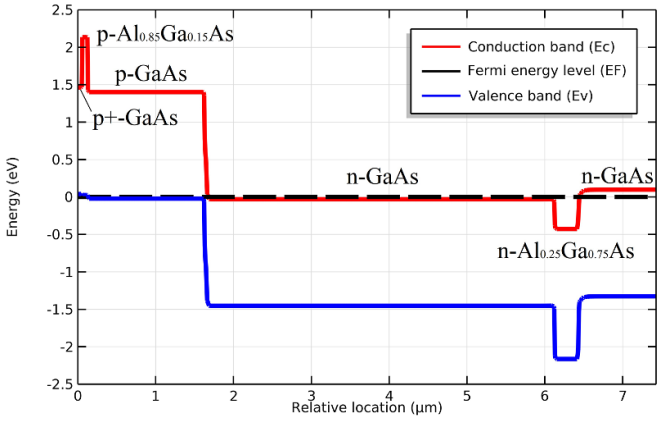

Figure 4. Energy diagram of the battery at thermodynamic equilibrium.

that is an increase of 37% over the battery without AlGaAs hole/electron transport layers (31.6 nW cm^{-2}). Figure 4 shows the energy diagram of the battery at thermodynamic equilibrium. The diffusion barrier formed by the band gap difference between the p-$Al_{0.85}Ga_{0.15}As$ window layer and p-GaAs emitter layer can inhibit the diffusion of minority electrons. The drift field formed between the n-$Al_{0.25}Ga_{0.75}As$ back surface layer and n-GaAs base layer, can accelerate the transport of radiation-induced minority carriers in the battery and improve the radiation-induced current.

3. Experiment

The GaAs/AlGaAs films used in our work were grown on the n-type GaAs substrates by MOCVD. The substrate impurity concentration is 2×10^{18} cm^{-3}. The p-type doped element is Zn, and the n-type doped element is Si. To fabricate the GaAs-based betavoltaic batteries on the planar GaAs-based wafer, firstly the photoresist on the surface of p^+-GaAs cap layer was patterned by photolithography and the development areas were used to prepare the ohmic contact. Then, the Ti/Pt/Au thin films with thickness of 260 nm were grown on the epitaxial chip by magnetron sputtering as the p-plane electrode. Next, the non-graphic electrode materials were removed by the Lift-off process. As the fourth step, the substrate thickness was reduced to 220 μm using the chemico mechanical planarization system. Finally, the Au/Ge/Ni thin films with thickness of 260 nm were grown as the n-plane electrode, followed by the metallization annealing step. After the chip scribing, the chips were adhered on the chip holder using Ag glue. To facilitate the electrical testing, the Au line bonding was performed between the p-plane electrode and transition electrode, followed by the wire bonding. The ^{63}Ni plate (3.1×1 cm^2) with an apparent activity density of 6 mCi cm^{-2} was placed 1.5 mm away from the energy converter in order not to make short-circuit. The photograph of the GaAs-based betavoltaic batteries is shown in figure 5. The size of the energy converter is 1×1 cm^2. Four kinds of comb-like electrodes were designed, including 2-busbar, 3-busbar, 4-busbar and 5-busbar. The busbar width is 500 μm, the finger width is 50 μm, and the finger gap is 572 μm, all of which are based on the optimization of power loss [33].

4. Results and discussion

The photoluminescence (PL) spectrum of the GaAs-based films is shown in figure 6(a), which illustrates that there is a main peak located at 876.5 nm with FWHM (full width at half maxima) of 45.8 nm, corresponding to the GaAs PL peak. As the n-$Al_{0.25}Ga_{0.75}As$ back surface layer is deeply buried, the light emitted by it will be absorbed by GaAs, so its luminous peak cannot be observed. Figure 6(b) shows the x-ray diffraction rocking curves of the GaAs-based films. The peak at 66.05 degrees corresponds to the GaAs substrate, the second peak on the left is the 0.3 μm-thick $Al_{0.25}Ga_{0.75}As$ peak, and the leftmost peak corresponds to the $Al_{0.85}Ga_{0.15}As$ layer only 0.08 μm-thick.

The fabricated GaAs-based betavoltaic batteries were characterized by using an Electrochemical Analyzer (CHI604D). And the measurements were made under dark condition in a Faraday cage. Figure 7 shows the change of current–voltage (*I–V*) characteristic between dark and irradiation conditions of the battery with 2-busbar comb-like electrode, and the inset gives the current values near zero bias. It can be seen that the battery exhibits a remarkable betavoltaic effect under the

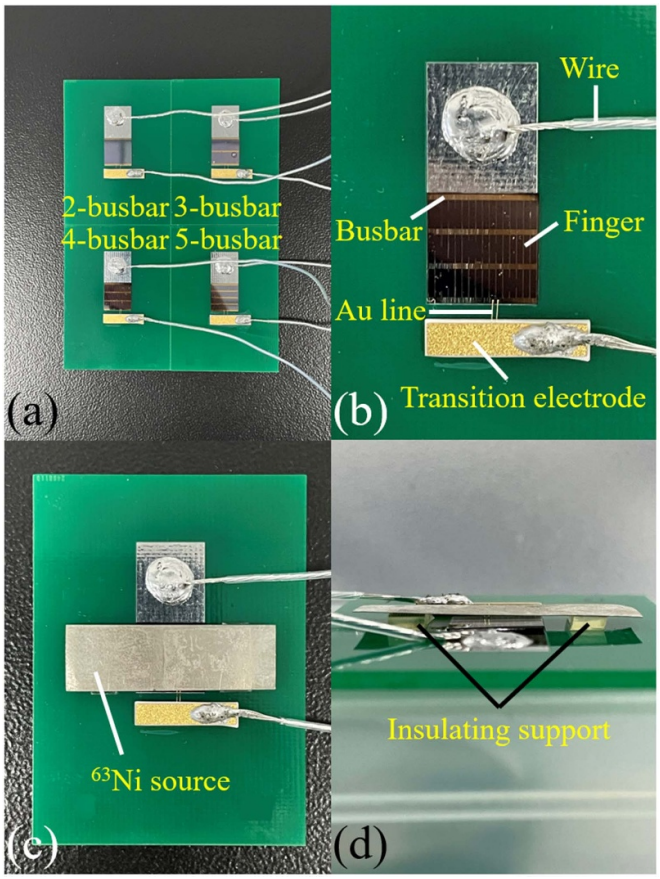

Figure 5. Photograph of the GaAs-based betavoltaic batteries. (a) Four kinds of comb-like electrodes. (b) Energy converter structure. (c) Loading ^{63}Ni source, overhead view. (d) Loading ^{63}Ni source, side view.

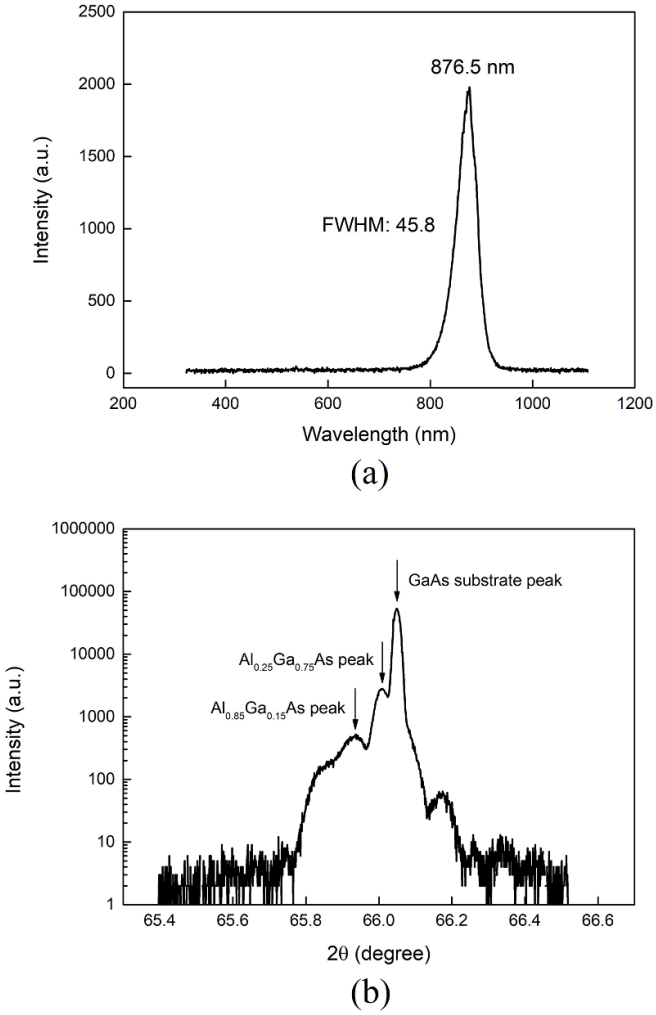

Figure 6. (a) PL spectrum, (b) XRD rocking curves of the GaAs-based films.

irradiation of ^{63}Ni source, and a short-circuit current density (J_{sc}) of 9.3 nA cm^{-2}, an open-circuit voltage (V_{oc}) of 55 mV are obtained. However, the measured J_{sc} and V_{oc} of the fabricated battery are far apart from its optimal designed values (J_{sc} = 85.6 nA cm^{-2} and V_{oc} = 0.67 V). For the poor output, the possible reasons are as follows: (1) Due to the decay, the real apparent activity density of the ^{63}Ni source used in the measurements is not 6 mCi cm^{-2} as used in the simulation model, and fewer electron–hole pairs are actually generated in the energy converter. (2) The beta particles are absorbed in the air (1.5 mm thick) and p-plane electrode (shadowing loss of 17.65%). (3) The substrate of the energy converter is too thick (220 μm), it is not conductive to the carrier transport and collection. (4) The device-area of 1 × 1 cm^2 is too big for the energy converter, so that the surface recombination of carriers cannot be ignored, which is not taken into account in the simulations. (5) According to the slope of I–V characteristic curve at V = 0 V under irradiation condition, the shunt resistance (R_{sh}) can be calculated as 7.61 × 10^6 Ω·cm^2. The low shunt resistance could be associated with the interface defects that provide an alternative current pathway with a low resistance.

Figure 8 shows the J_{sc}, V_{oc} and P_m of the GaAs-based betavoltaic batteries with four kinds of comb-like electrodes. Due to the shadowing loss (2-busbar: 17.65%, 3-busbar: 22.23%, 4-busbar: 26.80% and 5-busbar: 31.38%), the J_{sc} shows a decreasing trend when the number of busbars increases. It is observed that the battery with 3-busbar electrode has the lowest V_{oc}, which can be explained considering the dependence of open-circuit voltage (V_{oc}) on the short-circuit current density (J_{sc}) and reverse saturation current density (J_0). For an ideal p–n junction battery, the open-circuit voltage (V_{oc}) can be expressed as [21]:

$$V_{oc} = \frac{nkT}{q}\ln\left(\frac{J_{sc}}{J_0}+1\right), \tag{12}$$

where n is the ideal factor. Obviously, the V_{oc} increases with the increase of J_{sc} or with the decrease of J_0. The battery with 3-busbar electrode has the lowest V_{oc} but has a rather large J_{sc}, suggesting that J_{sc} is not the main cause of the low V_{oc} but J_0 is. To further confirm it, we extracted the J_0 for the battery via fitting the dark I–V characteristic curve using the following equation [15]:

$$\ln I = \frac{q}{nkT}V + \ln I_0, \tag{13}$$

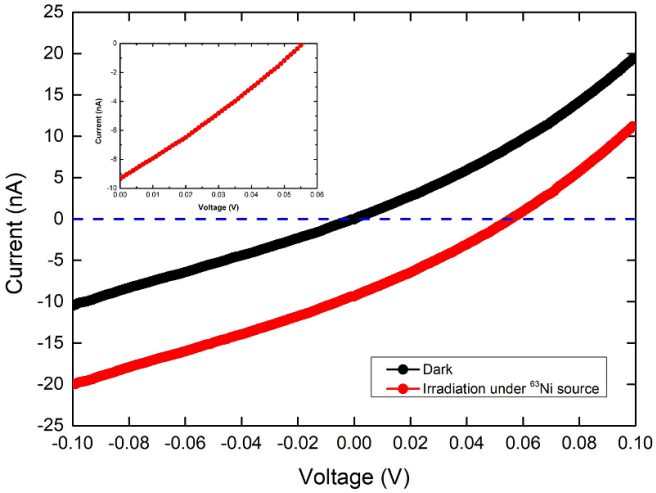

Figure 7. *I–V* characteristics of the GaAs-based betavoltaic battery with 2-busbar comb-like electrode in the dark and under ^{63}Ni source irradiation.

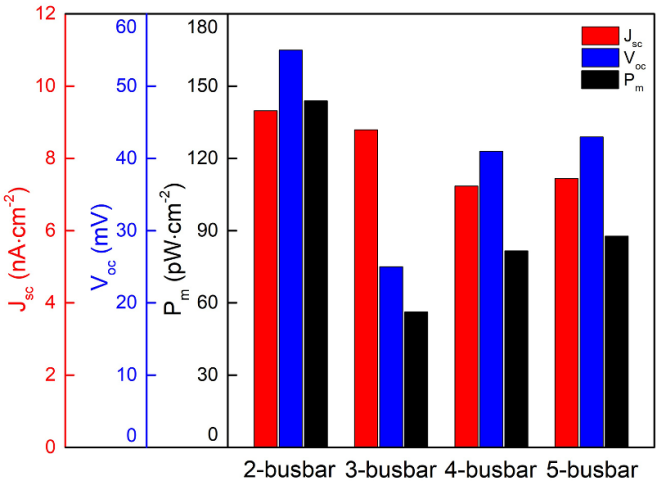

Figure 8. J_{sc}, V_{oc} and P_m of the GaAs-based betavoltaic batteries with four kinds of comb-like electrodes.

where I_0 is the reverse saturation current, and it can be given by the intercept of the curve on the Y-axis. The battery with 3-busbar electrode has the largest J_0 of 1.6 nA cm^{-2}, followed by the battery with 4-busbar electrode (0.9 nA cm^{-2}). The larger J_0 means the higher carrier recombination, which is attributed to the unsatisfactory preparation process. For example, when metal electrodes badly contact on the p$^+$-GaAs layer, the defects at p$^+$-GaAs/electrode interface as recombination centers lead to the high J_0. Therefore, the low V_{oc} for the battery with 3-busbar electrode is due to the high carrier recombination resulting in high J_0. Ultimately, the batteries with 2-busbar and 5-busbar electrode have the largest P_m (143.9 pW cm^{-2} and 87.8 pW cm^{-2}).

The measurements were also made at a low temperature range of 233.15–253.15 K in a high-low temperature test chamber. As shown in figure 9, the J_{sc} of the battery with 2-busbar comb-like electrode increases with temperature,

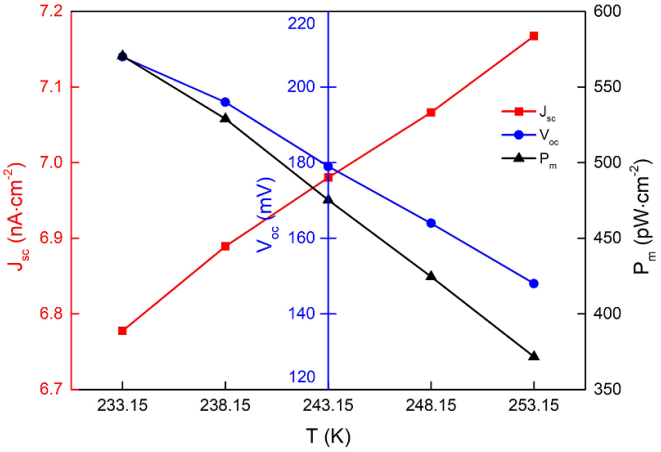

Figure 9. Changes in J_{sc}, V_{oc} and P_m as a function of temperature for the GaAs-based betavoltaic battery with 2-busbar comb-like electrode.

which can be attributed mainly to the decrease in semiconductor band gap with increasing temperature. The average energy dissipated per electron–hole pair generated decreases, while the number of electron–hole pairs increases. And this dependence of J_{sc} from temperature agrees with other experimental studies of GaAs-based betavoltaic batteries reported in literature [15]. Also similar to their studies, when the temperature increases, the V_{oc} drops sharply. This observation can be explained considering the higher intrinsic carrier concentration and larger reverse saturation current density. Finally, the P_m shows a decreasing trend with increasing temperature. At 233.15 K, the largest V_{oc} and P_m are 208 mV and 570.5 pW cm^{-2}, respectively, which increase by 278% and 296% compared with those measured at room temperature (300 K).

The comparison between our results and previous works of the GaAs-based betavoltaic batteries is shown in table 2. Although the final results of experiment show that the J_{sc} of GaAs-based batteries is only about 10 nA cm^{-2} as reported in the literatures, and the V_{oc} ranges from tens to hundreds of millivolts. The theoretical predictions indicate that the batteries with hole/electron transport layers proposed in this work can effectively enhance the output performance. Under the irradiation of a 6 mCi cm^{-2} ^{63}Ni source, the GaAs-based battery is expected to achieve a J_{sc} of 85.6 nA cm^{-2}, a V_{oc} of 0.67 V and a P_m of 43.3 nW cm^{-2}. The theoretical value of energy conversion efficiency of the developed battery is 6.21%, while the experimental values of energy conversion efficiency are 0.02% at 300 K and 0.08% at 233.15 K. Further improvements in fabrication process are needed to reduce the gap between experiment and prediction. And it is necessary to consider the theoretical optimization results when fabricating a betavoltaic battery. In addition, considering only the effective portion of radioisotope source and semiconductor energy converter, the power density of the fabricated GaAs-based betavoltaic battery is 4.86 nW g^{-1}. Due to the long half-life of ^{63}Ni source (100.2 years), the energy density of the battery can reach to 22.2 J g^{-1}. This suggests that the betavoltaic batteries have broad application prospects.

Table 2. Comparison between our results and previous works of the GaAs-based betavoltaic batteries.

Structure	Radioisotope	J_{sc} (nA cm^{-2})	V_{oc} (mV)	P_m (nW cm^{-2})	Method	Reference
P^+PINN^+	^{63}Ni (10 mCi cm^{-2})	0.36 (300 K)	324 (300 K)	0.071 (300 K)	Experiment	[14]
PN	^{63}Ni (4.889 mCi cm^{-2})	11 (333.15 K)	470 (213.15 K)	—	Experiment	[15]
PIN	^{63}Ni (10.2 mCi cm^{-2})	21 (−20 °C)	200 (−20 °C)	1.4 (−20 °C)	Experiment	[16]
p–n junction with	^{63}Ni (6 mCi cm^{-2})	9.3 (300 K)	55 (300 K)	0.14 (300 K)	Experiment	Our work
hole/electron		6.8 (233.15 K)	208 (233.15 K)	0.57 (233.15 K)		
transport layers		85.6 (300 K)	670 (300 K)	43.3 (300 K)	Theory	

5. Conclusion

In summary, the GaAs-based betavoltaic batteries with AlGaAs hole/electron transport layers were demonstrated in our work, which have more favorable band structure for the transport and collection of radiation-induced carriers. The Monte Carlo codes and COMSOL Multiphysics were combined to predict the output performance of batteries and optimize the structure parameters of energy converter. And the optimized GaAs-based battery with ^{63}Ni source was expected to achieve a J_{sc} of 85.6 nA cm^{-2}, a V_{oc} of 0.67 V and a P_m of 43.3 nW cm^{-2}. Next, the GaAs/AlGaAs films were grown on GaAs substrate by MOCVD, and a ^{63}Ni source with apparent activity density of 6 mCi cm^{-2} was loaded to fabricate the betavoltaic batteries. The I–V characteristics showed that the J_{sc} of the battery with 2-busbar comb-like electrode can reach to 9.3 nA cm^{-2}, and due to the shadowing loss, it shows a decreasing trend when the number of busbars increases. The largest V_{oc} of 55 mV and P_m of 143.9 pW cm^{-2} can be achieved on the battery with 2-busbar electrode, followed by the battery with 5-busbar electrode. Furthermore, the tests in the temperature range of 233.15–253.15 K showed that the battery performance is significantly improved at low temperature. At 233.15 K, the V_{oc} and P_m of the battery with 2-busbar electrode were increased by 278% and 296%, respectively, compared to room temperature (300 K). Due to the possible reasons in epitaxial growth, device packaging and measurement error, the actual output performances of the batteries are lower than the theoretical predictions. It is expected to reduce the gap between them by improving the battery preparation technologies, such as high-quality epitaxial growth, substrate thinning and surface passivation techniques. And the optimized structure of energy converter proposed in this work is promising for improving the performance of GaAs-based betavoltaic batteries. Moreover, the power density of betavoltaic batteries can be further improved by using the high-energy β sources (and the radiation damage needs to be considered), and increasing the source activity density. In addition, using the wider band gap semiconductors is also beneficial to improve the battery efficiency.

Data availability statement

The data that support the findings of this study are available from the corresponding author upon reasonable request.

Acknowledgments

This work was supported by the National Natural Science Foundation of China (Nos. 11075064 and U1867210) and the National Major Scientific Instruments and Equipment Development Projects (No. 2012YQ240121).

Conflict of interest

The authors have no conflicts to disclose.

ORCID iDs

Renzhou Zheng https://orcid.org/0000-0003-0913-7997
Jingbin Lu https://orcid.org/0000-0002-7518-7637
Yu Wang https://orcid.org/0000-0002-4100-4177
Xiaoyi Li https://orcid.org/0000-0002-2193-6049

References

[1] Prelas M A, Weaver C L, Watermann M L, Lukosi E D, Schott R J and Wisniewski D A 2014 A review of nuclear batteries *Prog. Nucl. Energy* **75** 117–48
[2] Olsen L C, Cabauy P and Elkind B J 2012 Betavoltaic power sources *Phys. Today* **65** 35–38
[3] Lu M, Zhang G G, Fu K, Yu G H, Su D and Hu J F 2011 Gallium nitride Schottky betavoltaic nuclear batteries *Energy Convers. Manage.* **52** 1955–8
[4] Prelas M A, Boraas M, Aguilar F D, Seelig J D, Tchouaso M T and Wisniewski D 2016 *Nuclear Batteries and Radioisotopes* (*Lecture Notes in Energy* vol 56) (Cham: Springer Press)
[5] Wagner D L, Novog D R and Lapierre R R 2020 Design and optimization of nanowire betavoltaic generators *J. Appl. Phys.* **127** 244303
[6] Zhao C, Liao F Y, Liu K Z and Zhao Y Y 2021 Breaking the myth: wide-bandgap semiconductors not always the best for betavoltaic batteries *Appl. Phys. Lett.* **119** 153904
[7] Spencer M G and Alam T 2019 High power direct energy conversion by nuclear batteries *Appl. Phys. Rev.* **6** 031305
[8] Bower K, Barbanel Y, Shreter Y and Bohnert G 2002 *Polymers, Phosphors and Voltaics for Radioisotope Microbatteries* (Boca Raton, FL: CRC Press) p 352
[9] Neamen D A 2017 *Semiconductor Physics and Devices: Basic Principles* 4th edn (Xi'an: Publishing House of Electronics Industry, McGraw-Hill Education) pp 248–630
[10] Chen H Y, Yin J H and Li D R 2011 Electrode pattern design for GaAs betavoltaic batteries *J. Semicond.* **32** 084006

[11] Chen H Y, Jiang L and Li D R 2011 Measurement of beta particles induced electron-hole pairs recombination in depletion region of GaAs PN junction *Chin. Phys. Lett.* **28** 058101
[12] Chen H Y, Jiang L and Chen X Y 2011 Design optimization of GaAs betavoltaic batteries *J. Phys. D: Appl. Phys.* **44** 215303
[13] Bouzid F, Dehimi S, Hadjab M, Saeed M A and Pezzimenti F 2021 Performance prediction of AlGaAs/GaAs betavoltaic cells irradiated by nickel-63 radioisotope *Physica* B **607** 412850
[14] Li D R, Jiang L, Yin J H, Tan Y Y and Lin N 2012 Betavoltaic battery conversion efficiency improvement based on interlayer structure *Chin. Phys. Lett.* **29** 078102
[15] Wang H, Tang X B, Liu Y P, Xu Z H, Liu M and Chen D 2015 Temperature effect on betavoltaic microbatteries based on Si and GaAs under ^{63}Ni and ^{147}Pm irradiation *Nucl. Instrum. Methods Phys. Res.* B **359** 36–43
[16] Butera S, Lioliou G and Barnett A M 2017 Temperature effects on gallium arsenide ^{63}Ni betavoltaic cell *Appl. Radiat. Isot.* **125** 42–47
[17] Khvostikov V P, Kalinovskii V S, Sorokina S V, Khvostikova O A and Andreev V M 2019 Tritium power supply sources based on AlGaAs/GaAs heterostructures *Tech. Phys. Lett.* **45** 1197–9
[18] Dorokhin M V *et al* 2022 GaAs diodes for TiT_2-based betavoltaic cells *Appl. Radiat. Isot.* **179** 110030
[19] Fonash S 2016 *Solar Cell Device Physics* (New York: Elsevier, Inc.) pp 102–10
[20] Bouzid F, Pezzimenti F and Dehimi L 2020 Modelling and performance analysis of a GaN-based n/p junction betavoltaic cell *Nucl. Instrum. Methods Phys. Res.* A **969** 164103
[21] Zhao C, Lei L, Liao F Y, Yuan D P and Zhao Y Y 2020 Efficiency prediction of planar betavoltaic batteries basing on precise modeling of semiconductor units *Appl. Phys. Lett.* **117** 263901
[22] Zandi S, Saxena P, Razaghi M and Gorji N E 2020 Simulation of CZTSSe thin-film solar cells in COMSOL: three-dimensional optical, electrical and thermal models *IEEE J. Photovolt.* **10** 1503–7
[23] Zandi S, Saxena P and Gorji N E 2020 Numerical simulation of heat distribution in RGO-contacted perovskite solar cells using COMSOL *Sol. Energy* **197** 105–10
[24] Zheng R Z *et al* 2021 Investigation of carrier transport and collection characteristics for GaAs-based betavoltaic batteries *AIP Adv.* **11** 105108
[25] Takahashi K, Yamada S, Unno T and Kuma S 1998 Characteristics of GaAs solar cells on Ge substrate with a preliminary grown thin layer of A1GaAs *Sol. Energy Mater. Sol. Cells* **50** 169–76
[26] Xie B S, Dai P, Luo X D and Liu S L 2017 IV characteristics and analysis for GaAs based single junction solar cells with different back surface fields *Acta Opt. Sin.* **37** 223002
[27] Klein C A 1968 Bandgap dependence and related features of radiation ionization energies in semiconductors *J. Appl. Phys.* **39** 2029–38
[28] Adachi S 1985 GaAs, AlAs and $Al_xGa_{1-x}As$: material parameters for use in research and device applications *J. Appl. Phys.* **58** R1
[29] Li X F, Hylton N P, Giannini V, Lee K H, Ekins-Daukes N J and Maier S A 2013 Multi-dimensional modeling of solar cells with electromagnetic and carrier transport calculations *Prog. Photovolt., Res. Appl.* **21** 109–20
[30] Bednar N, Severino N and Adamovie N 2015 Optical simulation of light management in CIGS thin-film solar cells using finite element method *Appl. Sci.* **5** 1735–44
[31] Sotoodeh M, Khalid A H and Rezazadeh A A 2000 Empirical low-field mobility model for III–V compounds applicable in device simulation codes *J. Appl. Phys.* **87** 2890–900
[32] Lundstrom M S, Klausmeier-Brown M E, Melloch M R, Ahrenkiel R K and Keyes B M 1990 Device-related material properties of heavily doped gallium arsenide *Solid-State Electron.* **33** 693–704
[33] Ren L, Wang Q, Zhang D, Lu C and Du X G 2013 Optimum design of metal electrodes of silicon solar cell *Acta Energ. Sol. Sin.* **34** 1746–9